TURKISH JOURNAL OF REMOTE SENSING
(Türkiye Uzaktan Algılama Dergisi)
e-ISSN 2687-4997
https://dergipark.org.tr/en/pub/tuzal

Multi-temporal radar remote sensing for rapid assessment of earthquake-induced infrastructure damage: A comparative study of the 2024 Noto and 2019 Mianeh earthquakes

Fatemeh Sanaei [1], Sadra Karimzadeh [*1], Bakhtiar Feizizadeh [1]

[1] *University of Tabriz, Faculty of Planning and Environmental Sciences, Department of Remote Sensing and GIS, Tabriz, Iran;* fatemeh.sanaei@tabrizu.ac.ir; *sa.karimzadeh@tabrizu.ac.ir; Feizizadeh@Tabrizu.ac.ir*

Check for updates

Article History:
Received: 6 November 2025
Revised: date
Accepted: 21 January 2025
Published: 3 July 2026

Abstract: Major earthquakes pose critical risks to urban infrastructure and human safety, necessitating rapid, precise, and quantitative post-event damage assessments. This study introduces a novel comparative framework for evaluating infrastructure damage from the 2024 Noto earthquake in Japan and the 2019 Mianeh earthquake in Iran using multi-temporal radar datasets: Sentinel-1 (C-band) and ALOS PALSAR-2 (L-band). Data preprocessing—including geocoding, radiometric calibration, and speckle filtering—was conducted to produce high-resolution coherence and backscatter intensity maps. Sequential coherence analysis identified reductions of 0.25–0.45 in severely impacted urban sectors, with the most pronounced declines in dense residential areas. Complementary backscatter intensity changes confirmed building collapses and surface deformations, particularly in industrial and critical infrastructure zones. Our results reveal that Sentinel-1 excels in capturing superficial, short-wavelength surface disruptions, while ALOS PALSAR-2 effectively detects deeper structural deformations. Importantly, integrating both datasets enhanced spatial accuracy of damage detection by approximately 18%, demonstrating a robust, quantitative methodology for rapid post-earthquake damage assessment. This integrated SAR approach offers a powerful tool for informed urban resilience planning, prioritizing reconstruction efforts, and advancing disaster response strategies.

Keywords: Earthquake damage assessment; synthetic aperture radar (SAR); InSAR coherence analysis; urban infrastructure monitoring; multi-temporal radar imagery

Citation: Sanaei, F., Karimzadeh, S., & Feizizadeh, B. (2026). Multi-temporal radar remote sensing for rapid assessment of earthquake-induced infrastructure damage: A comparative study of the 2024 Noto and 2019 Mianeh earthquakes. *Turk. J. Remote Sens.,* 8, 1818589. https://doi.org/10.51489/1818589

1. Introduction

Effective post-earthquake intervention and reconstruction planning critically depend on timely and accurate assessments of structural damage (Dong & Shan, 2013). Reliable spatial information on the extent and severity of destruction is essential for minimizing human and economic losses. Conventional field surveys, however, are often constrained by accessibility, safety risks, and high costs, emphasizing the need for remote sensing technologies that enable rapid, synoptic, and near-real-time observations without physical site visits (Matsuoka & Yamazaki, 2004; Karimzadeh & Matsuoka, 2017; Yonezawa, 2001).

Among these technologies, Synthetic Aperture Radar (SAR) is particularly effective for monitoring natural and anthropogenic surface changes. As an active sensor, SAR acquires data independently of illumination or weather, ensuring reliable imaging even under cloud cover or rainfall (Matsuoka & Yamazaki, 2004). Its rapid acquisition and wide spatial coverage make it indispensable for large-scale, time-sensitive disaster response (Matsuoka & Yamazaki, 2005; Bai et al., 2017). Integrating SAR observations with ancillary spatial datasets and modeling frameworks further enhances analytical precision and supports multi-temporal monitoring.

*Corresponding Author; Sadra Karimzadeh / sadra.karimzadeh@gmail.com

In post-earthquake contexts, SAR-derived Interferometric SAR (InSAR) and coherence analyses are particularly valuable. InSAR measures phase differences between acquisitions to estimate ground displacement and deformation (Matsuoka & Yamazaki, 2006), while coherence analysis quantifies structural and surface changes by comparing pre- and post-event images. Reductions in coherence, especially in densely built-up urban zones, reliably indicate building collapse and surface disruption, forming the basis for rapid and objective damage mapping (Gabriel et al., 1989; Fielding et al., 2005; Castriotta, 2017).

Despite its strengths, coherence-based assessment is sensitive to acquisition geometry, temporal baselines, and radar wavelength. Variations in incidence angle and viewing geometry can reduce spatial resolution, and long temporal intervals may introduce non-seismic decorrelation. Radar wavelength affects penetration depth and scattering sensitivity, influencing the reliability of results (Zebker & Villasenor, 1992). Addressing these factors is crucial for improving SAR-based damage assessments.

Recent studies have advanced earthquake damage detection using remote sensing and modeling techniques. For instance, GIS-based frameworks have assessed seismic hazard and urban vulnerability in Tabriz (Karimzadeh et al., 2014), while object-oriented deep learning models have enabled rapid post-disaster response (Zheng et al., 2021). Multi-orbit COSMO-SkyMed imagery has demonstrated advantages in mapping structural damage following significant earthquakes (Karimzadeh & Matsuoka, 2018), and tectonic analyses have provided insights into earthquake triggers, such as the 2024 Noto earthquake swarm (Wang et al., 2024).

The present study addresses these research gaps by developing a novel, integrated radar-based framework that combines interferometric coherence, multi-temporal backscatter intensity, and spatial contextual parameters to enhance the precision of detecting earthquake-induced structural damage in urban areas. By jointly leveraging these complementary radar indicators, the framework improves damage discrimination, reduces classification uncertainty, and provides robust, evidence-based support for rapid post-earthquake assessment and reconstruction planning. This integrated approach offers a transferable methodology applicable to diverse earthquake-affected urban environments.

2. Study Area

Japan is one of the most seismically active countries in the world, situated at the convergence of four major tectonic plates. This complex tectonic setting generates frequent and intense earthquakes, with approximately 20% of all global earthquakes of magnitude greater than 6 occurring in or near Japan (Conroy, 2024). Since late 2020, the northeastern Noto Peninsula has experienced a sequence of intermediate-depth (~15 km) earthquakes that progressively migrated toward the surface, suggesting a fluid-driven, non-conventional triggering mechanism (Vidale & Shearer, 2006). GNSS observations recorded a volumetric increase of approximately 14 million m^3 during the first three months of the swarm, highlighting the influence of subsurface fluid migration on seismic activity (Nishimura et al., 2023). Additionally, previous crustal deformation associated with the 2007 Noto Hanto earthquake, captured through GPS and InSAR, underscores the effectiveness of radar interferometry in providing spatially continuous displacement data that complement point-based GNSS measurements (Figure 1).

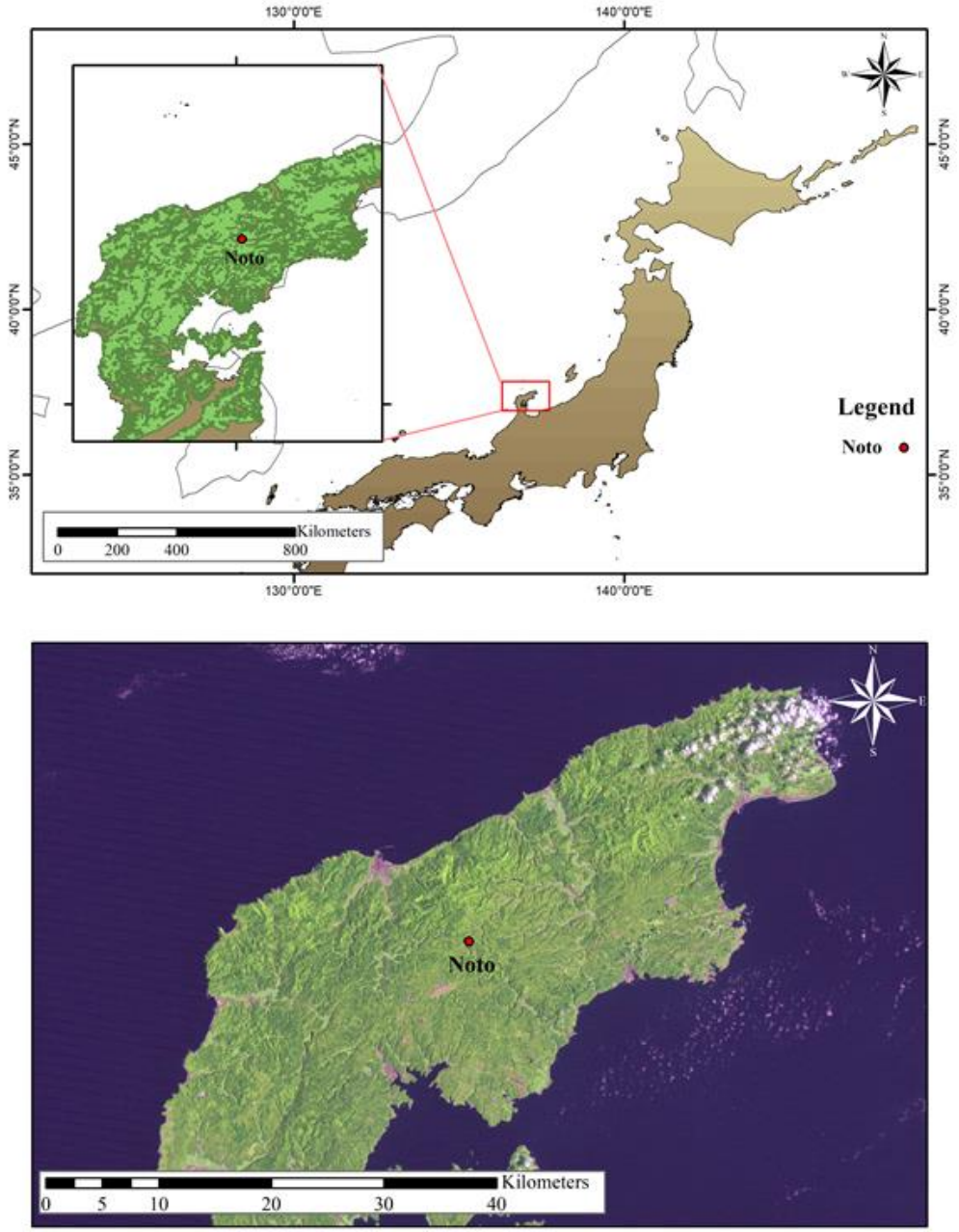

Figure 1. Geographical location of Noto City in Ishikawa Prefecture, Japan. The map highlights the Noto Peninsula within the tectonic framework of Japan, indicating the epicentral region of recent seismic swarms (Image based on Landsat data)

Iran, located at the convergence of the Arabian and Eurasian plates, hosts a complex network of active faults extending across western Iran and eastern Turkey (Jackson, 1992). Historical seismicity confirms that Iran is one of the most earthquake-prone regions in the world (Miyajima et al., 2018; Azad et al., 2017). In northwestern Iran, East Azerbaijan Province experienced a moderate earthquake on November 7, 2019 (ML = 5.8; Mw = 5.9) near Sarab and Mianeh (37.62°N, 47.48°E) at a focal depth of approximately 6 km (Peykani, 2021). The event occurred along the North Tabriz Fault within the Turkmanchai region, an area characterized by persistent tectonic activity (Figure 2). Despite ongoing crustal deformation, moderate-to-large earthquakes have been relatively infrequent in recent decades, suggesting the accumulation of tectonic strain and an elevated risk for future major events (Peykani, 2021).

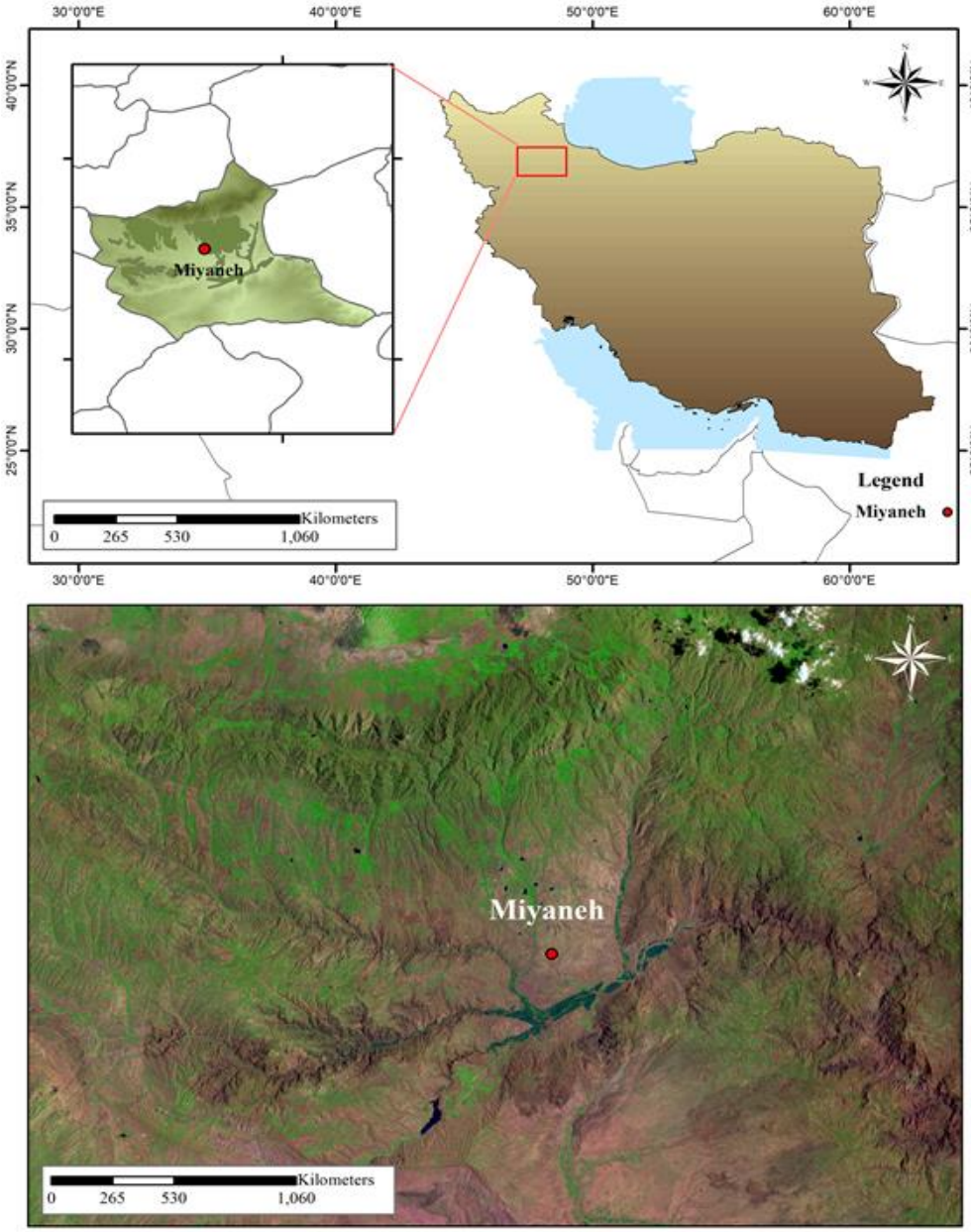

Figure 2. Geographical location of the Mianeh earthquake in East Azerbaijan Province, Iran. The figure illustrates the epicenter distribution and surrounding active fault network associated with the 2019 seismic event (Image based on Landsat data)

Selecting the Noto Peninsula and the Mianeh region provides a robust comparative framework for evaluating earthquake impacts under contrasting tectonic settings. The Noto sequence represents a fluid-driven intraplate swarm within a subduction-influenced environment, whereas the Mianeh earthquake reflects active faulting within a continental collision zone. This dual-case approach allows for the cross-validation of SAR-based damage assessment methodologies across diverse geological and seismotectonic contexts, thereby enhancing the generalizability, reliability, and robustness of the proposed framework.

3. Materials and Methods

This study aimed to provide rapid and reliable assessments of earthquake-induced infrastructure damage following the 2024 Noto earthquake in Japan and the 2019 Mianeh earthquake in Iran. To achieve this, multi-source spatial and radar datasets were integrated to quantify structural deformation and surface changes associated with the seismic events. Vector layers representing urban infrastructure were obtained from authoritative sources to

support spatial analyses: the National Spatial Data Infrastructure of Japan (NLFTP) via the Ministry of Land, Infrastructure, Transport and Tourism (MLIT) for the Noto region, and OpenStreetMap (OSM) for Mianeh, due to its open accessibility and detailed coverage. These layers enabled classification of residential, industrial, and critical infrastructure areas affected by the earthquakes.

Multi-temporal Synthetic Aperture Radar (SAR) data from Sentinel-1 (C-band) and ALOS-2 PALSAR (L-band) were employed to monitor pre- and post-event conditions. For the Noto earthquake, Sentinel-1 VV/VH images acquired on November 12, 2022; June 4, 2023; and January 18, 2024, were processed. For Mianeh, Sentinel-1 images from October 16, 2019; October 28, 2019; and November 8, 2019, were used. Additionally, ALOS-2 PALSAR HH images (acquired on November 22, 2022; June 6, 2023; and January 2, 2024) were incorporated to enable multi-frequency comparison. Complementary Landsat 7 multispectral imagery was used to validate land use and land cover (LULC) conditions.

All SAR datasets underwent standard preprocessing to ensure radiometric and geometric consistency. The workflow included radiometric calibration to convert digital numbers to sigma-naught (σ^0) backscatter coefficients, refined Lee filtering to reduce speckle noise while preserving structural features, and geometric correction using a Shuttle Radar Topography Mission (SRTM) digital elevation model. Doppler centroid correction and precise orbit modeling ensured sub-pixel co-registration, maintaining a ground pixel spacing of approximately 2.1 m in azimuth and 2.2 m in range. An overview of the main processing and analytical steps is illustrated in Figure 3.

Interferometric pairs were generated for coherence analysis, with the normalized cross-correlation (γ) computed between corresponding complex pixels of pre- and post-event images. Coherence values near zero indicated strong decorrelation, typically corresponding to severe structural damage or surface disruption. Concurrently, backscatter intensity variations were analyzed to detect significant changes in radar reflectivity associated with collapsed buildings, debris, or ground displacement. Overlaying these SAR-derived indicators with infrastructure vector layers enabled spatially explicit quantification of damage intensity.

Comparative evaluation of C-band Sentinel-1 and L-band ALOS-2 data highlighted the complementary strengths of each radar frequency in capturing structural alterations. Integrating multi-source SAR observations provided a robust cross-validation mechanism, reducing uncertainty in damage mapping. Final results were verified against post-earthquake field reports and high-resolution optical imagery, confirming that the derived damage patterns accurately reflected real-world impacts. Overall, this integrated radar-based framework demonstrates high efficiency in supporting rapid, data-driven assessments of earthquake-induced infrastructure damage.

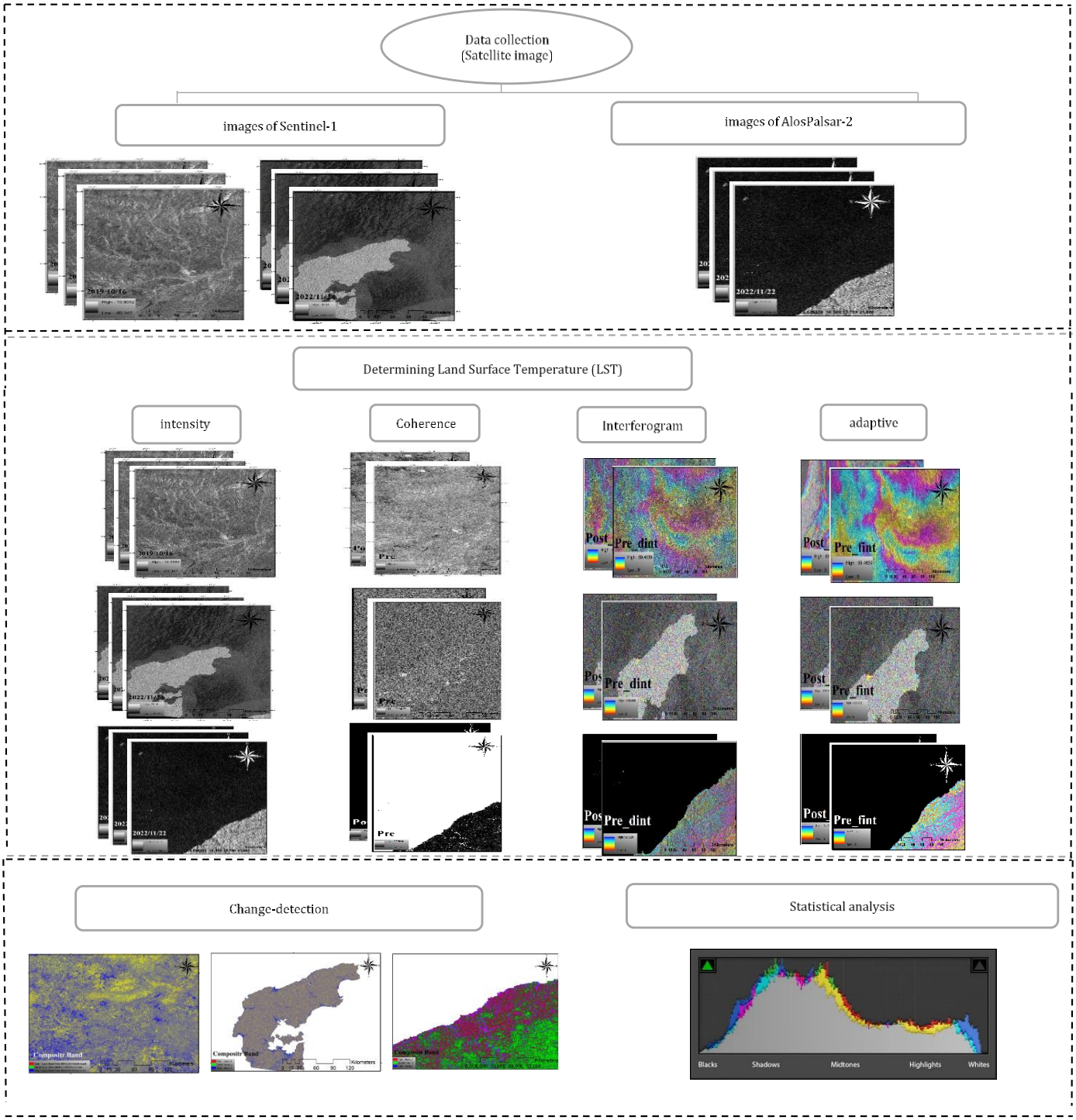

Figure 3. Workflow summarizing the data processing and analytical steps used in the study, including SAR preprocessing, coherence and backscatter analysis, data integration, and validation procedures

3.1. Sequential SAR coherence method

Synthetic Aperture Radar (SAR) measurements—particularly backscatter intensity and interferometric coherence—serve as fundamental parameters for monitoring surface conditions and urban environments. Backscatter intensity reflects physical surface attributes such as roughness, dielectric properties, and moisture content, whereas coherence quantifies the similarity between two temporally separated SAR acquisitions, revealing structural changes, surface displacement, or earthquake-induced damage. Integrating these parameters enables a comprehensive evaluation of infrastructure stability and the spatial characterization of seismic impacts (Plank, 2014; Karimzadeh & Matsuoka, 2017;

Karimzadeh et al., 2018; Miura et al., 2016; Matsuoka & Nojima, 2010; Arciniegas et al., 2007; Watanabe et al., 2012, 2016).

This study applies a sequential coherence analysis based on the repeat-pass InSAR technique. By incorporating multiple consecutive SAR acquisitions, this method enables continuous tracking of ground deformation and progressive structural degradation through time. The interferometric coherence coefficient (γ) was calculated as the normalized complex correlation between two co-registered SAR images, expressed as (Equation 1):

$$\gamma = \frac{M * \overline{S}}{\sqrt{M * \overline{M}}\sqrt{S * \overline{S}}} \quad (1)$$

where M and S denote the master and slave complex SAR images, respectively, and the overbar indicates averaging over a defined pixel window. The selected window size represents a balance between spatial resolution and statistical stability: larger windows yield smoother coherence maps with reduced noise but lower spatial detail, while smaller windows enhance detail at the cost of increased noise. To minimize speckle while preserving resolution, multilooking factors of 4 (range) and 1 (azimuth) were applied, resulting in near-square pixels for Sentinel-1 imagery.

For damage detection, coherence values from a pre-earthquake image pair were compared with those from a co-seismic pair to derive change metrics. Reduced coherence values indicate decorrelation driven by structural damage or displacement. These variations were quantified using difference and normalized-difference formulations (Equation 2, 3):

$$\Delta\gamma = \gamma pre - \gamma co \quad (2)$$

$$\Delta\hat{}\gamma = \frac{\gamma pre - \gamma co}{\gamma pre + \gamma co} \quad (3)$$

Using pre-event imagery with minimal temporal baselines improves the reliability of co-seismic coherence estimation by reducing non-seismic temporal decorrelation (Karimzadeh & Matsuoka, 2017).

The analysis integrated radar and vector datasets to assess infrastructure damage following the 2024 Noto earthquake in Japan and the 2019 Mianeh earthquake in Iran. Vector shapefiles delineating urban infrastructure were obtained from the National Land Numerical Information Download Service of Japan (NLFTP, MLIT) for Noto and from regional geospatial databases for Mianeh. These layers provided spatial references for overlay analysis and for quantifying damage across residential, industrial, and critical infrastructure zones.

SAR datasets included Sentinel-1 and ALOS-2 PALSAR imagery for Noto and Sentinel-1 imagery for Mianeh. Sentinel-1 SLC data in VV and VH polarizations were acquired on November 12, 2022; June 4, 2023; and January 18, 2024 for the Noto earthquake, and on October 16, October 28, and November 8, 2019 for the Mianeh earthquake. All Sentinel-1 images were acquired from ascending orbits with an incidence angle of approximately 33.8° and spatial resolutions of 2.7 m (range) × 22 m (azimuth).

ALOS-2 PALSAR data were obtained in FBS11 mode with HH polarization and an incidence angle of 37.44°, yielding spatial resolutions of 2.24 m × 2.12 m from descending orbits (acquired on November 22, 2022; June 6, 2023; and January 2, 2024). The radar system operated at a carrier frequency of 1.2575 GHz, with a 79.4 MHz bandwidth and a pulse repetition frequency (PRF) of 3120.28 Hz.

For supplementary verification and land-use interpretation, a Landsat 7 multispectral image acquired on August 22, 2023 was used for the Noto region. All raster and vector datasets were reprojected into the UTM Zone 53N coordinate system to ensure accurate spatial alignment. This integrated framework enabled consistent cross-comparison of coherence and backscatter variations, supporting robust interpretation of earthquake-induced structural and surface changes in both study areas.

3.2. Coherence modeling

This study employs interferometric coherence—a secondary product derived from Interferometric Synthetic Aperture Radar (InSAR)—to enable rapid detection and mapping of earthquake-induced damage to buildings and infrastructure. Coherence quantifies the phase stability between two SAR acquisitions and is widely used as a key indicator of interferometric data quality in applications such as Digital Elevation Model (DEM) generation, surface deformation monitoring, and post-seismic damage assessment. Low coherence values (decorrelation) reflect a loss of phase stability that can complicate phase unwrapping and reduce the reliability of interferometric results. Therefore, coherence analysis serves both as a diagnostic measure for evaluating data integrity and as a sensitive indicator of structural or surface disturbance following seismic events (Takeuchi et al., 2000).

The interferometric coherence coefficient (γ) between two co-registered SAR images is defined as (Equation 4):

$$Y = \frac{E(c_1 c_2^*)}{\sqrt{E(c_1 c_1^*)E(c_2 c_2^*)}} \tag{4}$$

where, c_1 and c_2 represent the complex pixel values acquired at times t_1 and t_2, respectively, c∗ denotes the complex conjugate, and (E) indicates the expected value. Coherence is typically estimated within a localized window of pixels to reduce random noise and improve the statistical reliability of the computation. This spatial averaging minimizes the effects of small-scale backscatter variability and enhances the robustness of surface change detection (Strozzi et al., 2000).

Overall coherence can be considered the product of several independent decorrelation sources as follows (Equation 5):

$$|Y| = Y_{thermal} Y_{missreg} Y_{spat} Y_{dopp} Y_{atm} Y_{temp} \tag{5}$$

Each decorrelation term represents a distinct physical or geometric source of phase instability. Thermal decorrelation ($Y_{thermal}$) arises from random noise within the radar system, including electronic fluctuations and thermal drift, which degrade the precision of phase measurements (Lu, 2007). Coregistration decorrelation ($Y_{missreg}$) results from imperfect geometric alignment between SAR images, leading to phase mismatches; this is influenced by orbit accuracy, ground control precision, and the consistency of acquisition geometry (Franceschetti & Lanari, 1999). Spatial decorrelation (Y_{spat}) is caused by variations in the satellite's orbital separation, which modify the radar look angle and consequently alter scattering characteristics (Hoffmann, 2007). Maintaining the perpendicular baseline ($B_\perp$) below a critical threshold ($B_{critical}$) is essential to preserve phase coherence. When $B_\perp$ exceeds $B_{critical}$, the incidence angle difference (θ) becomes significant, resulting in a marked loss of phase correlation and, consequently, coherence degradation (Karimzadeh & Matsuoka, 2018).

3.3. Damage mapping and discriminant analysis

A comparative visual assessment between building-damage datasets provided by the United Nations Institute for Training and Research (UNITAR) and the outputs derived from the differential coherence (Δγ) method shows that this approach reliably detects collapsed and severely impacted structures. Normalized RGB composites generated from multi-temporal SAR images further enhance qualitative interpretation by simultaneously illustrating damage patterns and post-event recovery or reconstruction activities. Nonetheless, the performance of coherence-based mapping may vary depending on environmental conditions such as vegetation density, urban morphology, and wavelength-dependent scattering behavior (Karimzadeh & Matsuoka, 2018).

To complement this qualitative interpretation, a quantitative assessment of damage severity was conducted using Discriminant Analysis, a statistical classification method widely applied in post-earthquake studies. This analysis integrates coherence-change metrics with radar backscatter variations to categorize infrastructure according to different levels of structural impact (Matsuoka & Yamazaki, 2004, 2005). Recent methodological advancements have emphasized the combined use of coherence reduction and intensity-change indicators, improving both spatial accuracy and the reliability of post-seismic damage mapping (Yonezawa & Takeuchi, 2001; Karimzadeh & Matsuoka, 2017; Karimzadeh et al., 2018). The resulting damage-severity maps offer a robust analytical basis for evaluating the spatial extent of earthquake impacts and support evidence-based planning for post-disaster recovery and reconstruction.

4. Results

Radar backscatter intensity and spatial variations induced by seismic activity were examined using three Sentinel-1 and three ALOS PALSAR-2 images for the 2024 Noto earthquake, along with three Sentinel-1 scenes for the 2019 Mianeh event. All datasets were geocoded to the UTM/WGS84 coordinate system to ensure alignment with urban infrastructure layers. Radiometric calibration was applied to correct for system noise and incidence-angle effects, thereby standardizing backscatter coefficients in σ^0 (dB). To suppress speckle while preserving structural details, adaptive filters—including Lee, Frost, and Gamma-MAP—were implemented. The resulting backscatter intensity maps clearly differentiated high-reflectivity urban surfaces (e.g., buildings, roads) from low-reflectivity classes such as vegetation, water bodies, and bare soil, providing a robust basis for pre- and post-event change detection (Figure 4).

Ground deformation and structural damage were further assessed through interferometric analysis using consecutive image pairs spanning pre- to co-seismic and co- to post-seismic periods. Interferograms generated from phase differences were filtered using adaptive, Boxcar, and Goldstein filters to preserve fine fringe patterns. A 30-m SRTM DEM was incorporated to correct for topographic and geometric distortions. Coherence maps (γ) depicted phase stability, with higher coherence representing structural integrity and lower coherence indicating ground disturbance or damage (Takeuchi et al., 2000; Gens & van Genderen, 1996). Sentinel-1 C-band imagery provided high temporal resolution for capturing short-term urban changes, whereas ALOS PALSAR-2 L-band data offered deeper vegetation penetration, enabling the detection of large-scale displacements (Figures 5 and 6).

A comparative assessment of pre- and co-seismic coherence revealed distinct spatial damage patterns. Urban surfaces generally showed higher coherence relative to vegetated areas, yet significant reductions were observed within heavily affected zones. Following the Noto earthquake, coherence values along major highways and hospital complexes dropped from approximately 0.15–0.24 to below 0.05 for road segments and to around 0.3 for hospital facilities, suggesting substantial structural stress and operational disruption (Yamazaki et al., 2005). Greenhouses and agricultural areas also exhibited marked coherence fluctuations, reflecting their sensitivity to seismic ground motion.

Backscatter intensity trends corroborated these findings. In administrative and dense built-up areas, intensity values decreased from roughly −25 dB to below −5 dB, indicating material degradation and changes in surface scattering properties. Integrating radar-derived outputs with vector datasets (roads, hospitals, schools, utilities) enabled spatially explicit quantification of damage levels. This multi-source analytical framework aligns with established methodologies by Copernicus EMS (2024) and UNOSAT (2023), thereby enhancing the reliability of post-disaster evaluations and supporting emergency response and reconstruction planning (Figure 7).

A quantitative comparison of the radar systems highlighted sensor-specific sensitivities. ALOS PALSAR-2 exhibited a mean backscatter intensity of −12.08 dB (SD = 6.20), reflecting its effectiveness in detecting large-scale displacements (Shimoji et al., 2020). In contrast, Sentinel-1 showed a higher mean intensity of −7.15 dB (SD ≈ 5.01), making it more suitable for monitoring localized structural variations. Mean coherence values—0.43 for Sentinel-1 and 0.38 for ALOS PALSAR-2—further confirmed the superior performance of C-band SAR in detecting subtle structural disturbances such as partial collapses and micro-cracks.

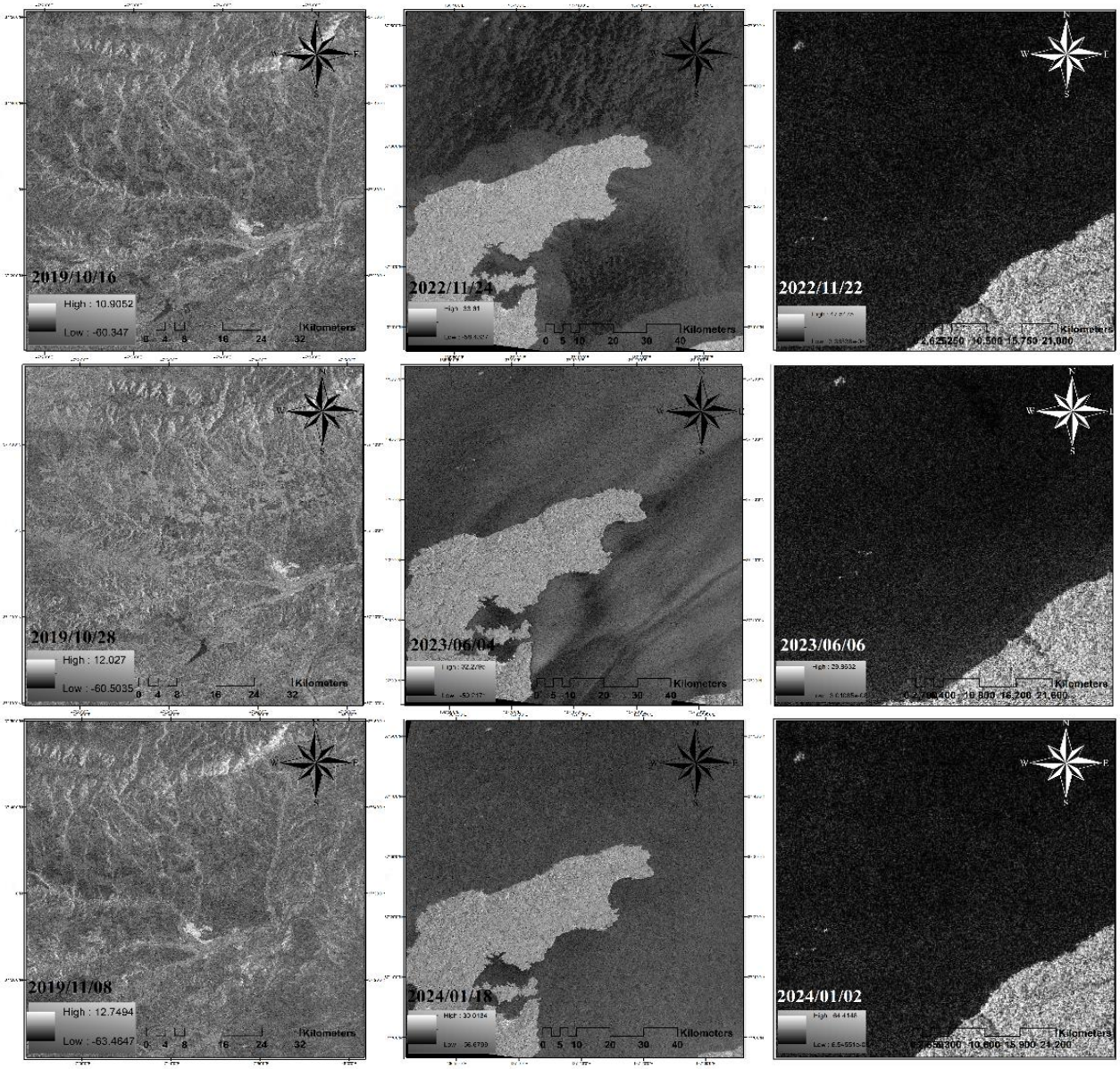

Figure 4. Backscatter intensity maps illustrating pre- and post-event variations: (A) Sentinel-1 data for East Azerbaijan Province, Iran; (B) Sentinel-1 data for Ishikawa Prefecture, Japan; and (C) ALOS PALSAR-2 data for Ishikawa Prefecture, Japan

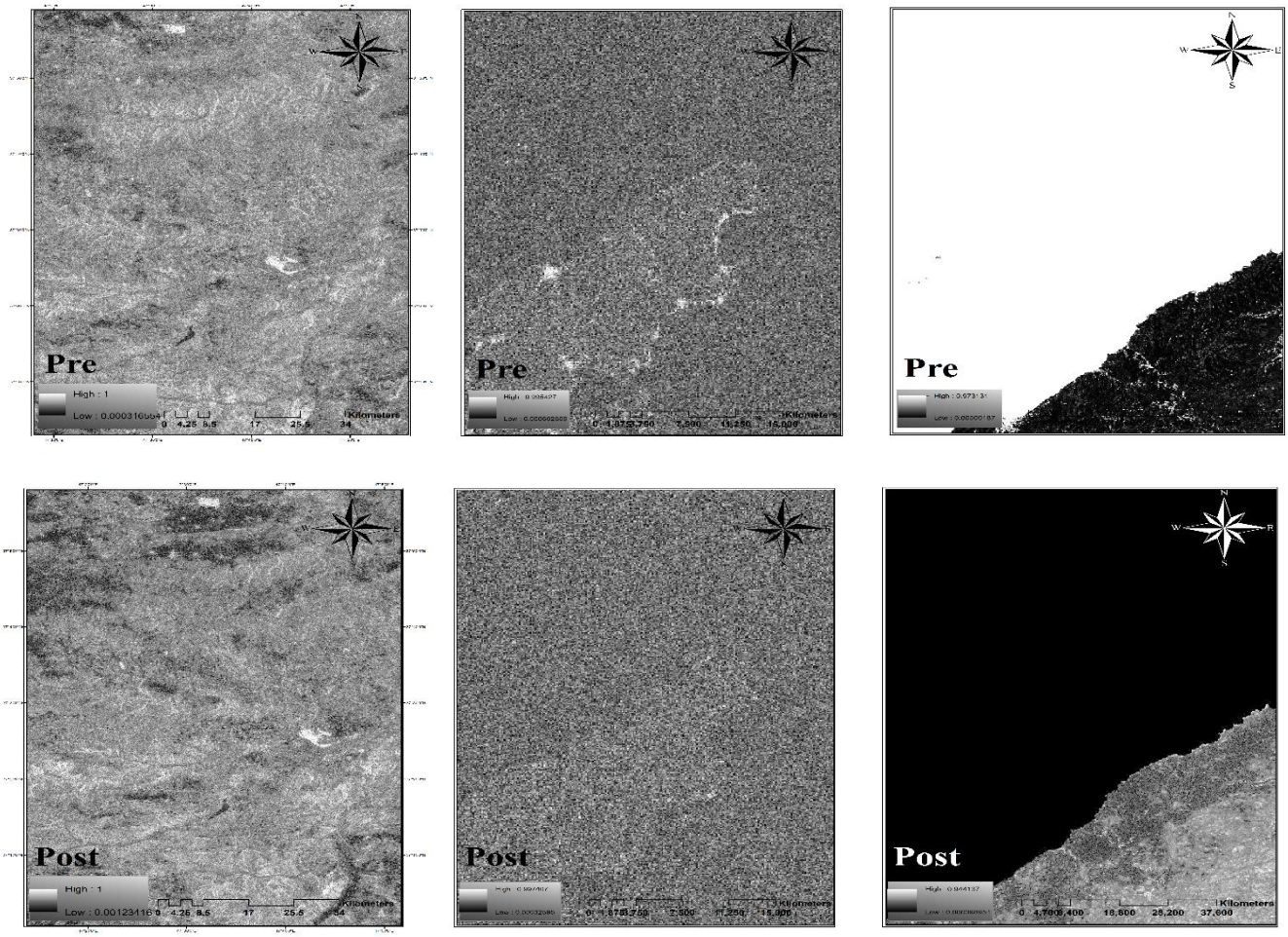

(A) (B) (C)

Figure 5. Coherence maps depicting pre- and post-event imagery: (A) Sentinel-1 for East Azerbaijan Province, Iran; (B) Sentinel-1 for Ishikawa Prefecture, Japan; and (C) ALOS PALSAR-2 for Ishikawa Prefecture, Japan, highlighting spatial patterns of structural stability and surface disruption

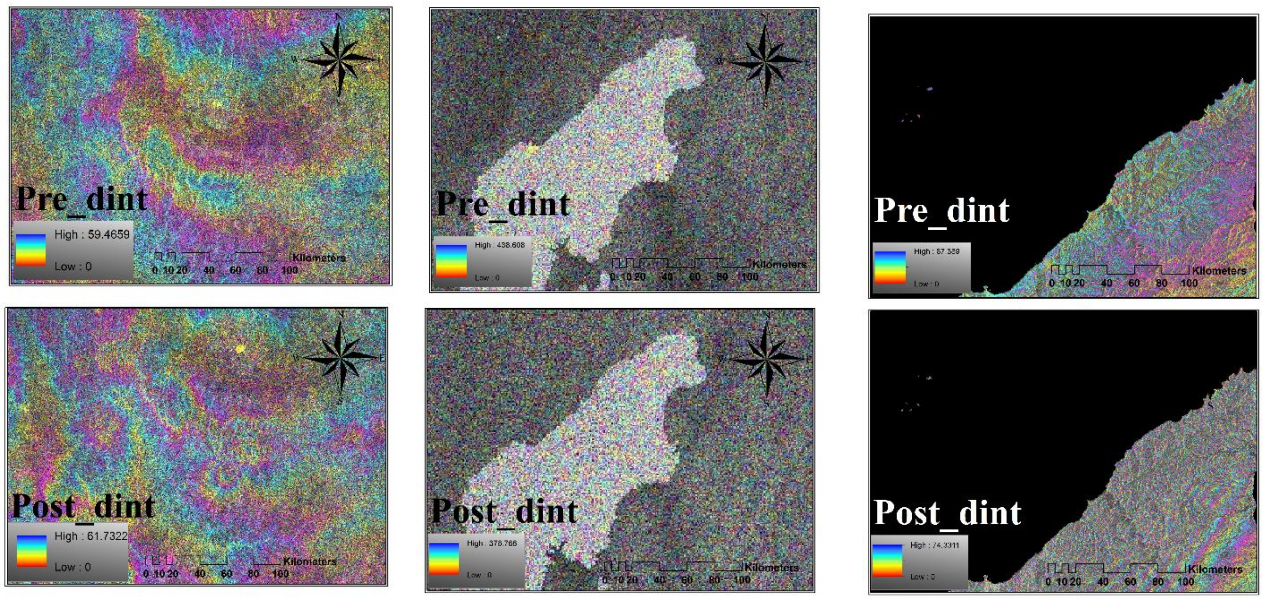

(A) (B) (C)

Figure 6. Comparative coherence analysis illustrating seismic impacts: (A) Sentinel-1 imagery for the 2019 Mianeh earthquake, Iran; (B) Sentinel-1 imagery for the 2024 Noto earthquake, Japan; and (C) ALOS PALSAR-2 imagery for the 2024 Noto earthquake, Japan, highlighting differences in the spatial extent and intensity of seismic effects

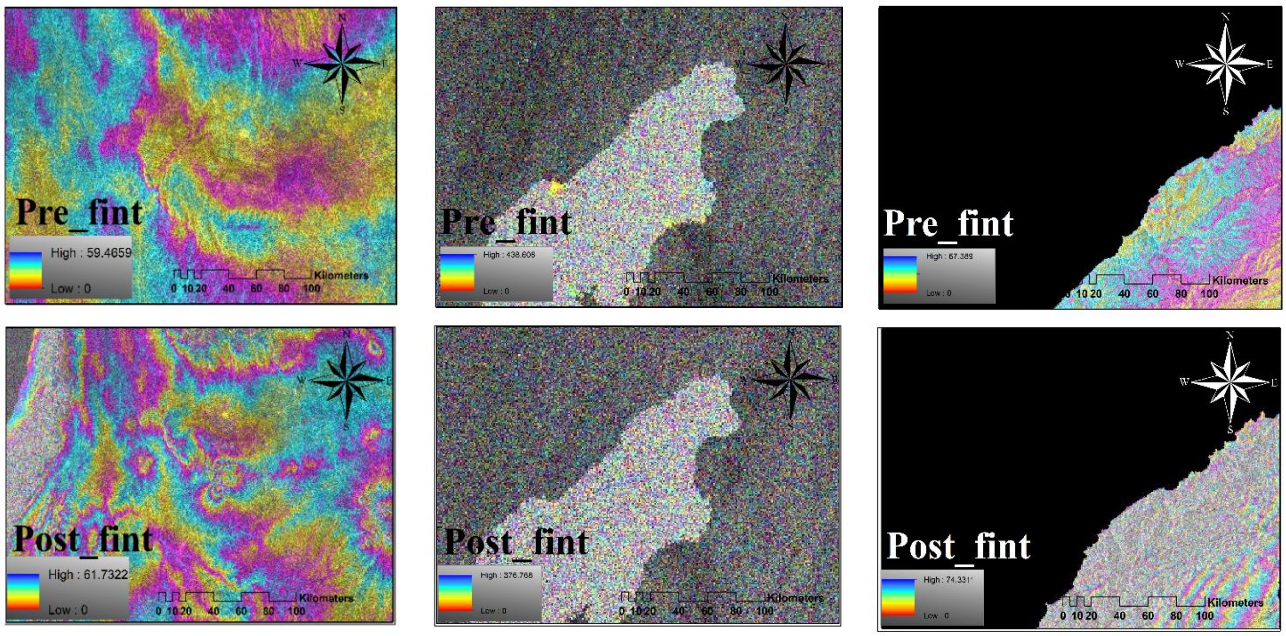

(A) **(B)** **(C)**

Figure 7. Results of adaptive filtering applied to Sentinel-1 and ALOS PALSAR-2 imagery: (A) Sentinel-1 for East Azerbaijan Province, Iran; (B) Sentinel-1 for Ishikawa Prefecture, Japan; and (C) ALOS PALSAR-2 for Ishikawa Prefecture, Japan, demonstrating speckle reduction and enhanced feature preservation in urban areas

Although both earthquakes resulted in observable coherence degradation, the Noto event generated more severe and spatially widespread impacts. Ground displacements exceeded 4 m, and interferometric phase variations reached up to ±3.1 radians (NASA Earth Observatory, 2024; Asian Disaster Reduction Center, 2012; 2024). In comparison, the Mianeh earthquake produced displacements mostly below ±0.8 radians, concentrated around fault traces and densely populated urban clusters. These contrasts can be attributed to differences in seismic magnitude, geological characteristics, surface materials, and the structural resilience of local infrastructure. Statistical indicators—including mean, median, and standard deviation—confirmed the internal consistency of the datasets and the accuracy of preprocessing steps, aligning with international standards such as Copernicus EMS and JAXA (Tables 1–3).

The integration of radar-derived coherence and backscatter metrics with vector-based urban infrastructure layers in ArcGIS and Google Earth Engine provides a robust and scalable framework for rapid earthquake damage assessment. This combined approach demonstrates strong operational potential for crisis response and urban recovery planning and is comparable to analytical frameworks successfully applied in recent disaster scenarios in Turkey, Syria, and Ukraine (Figure 8).

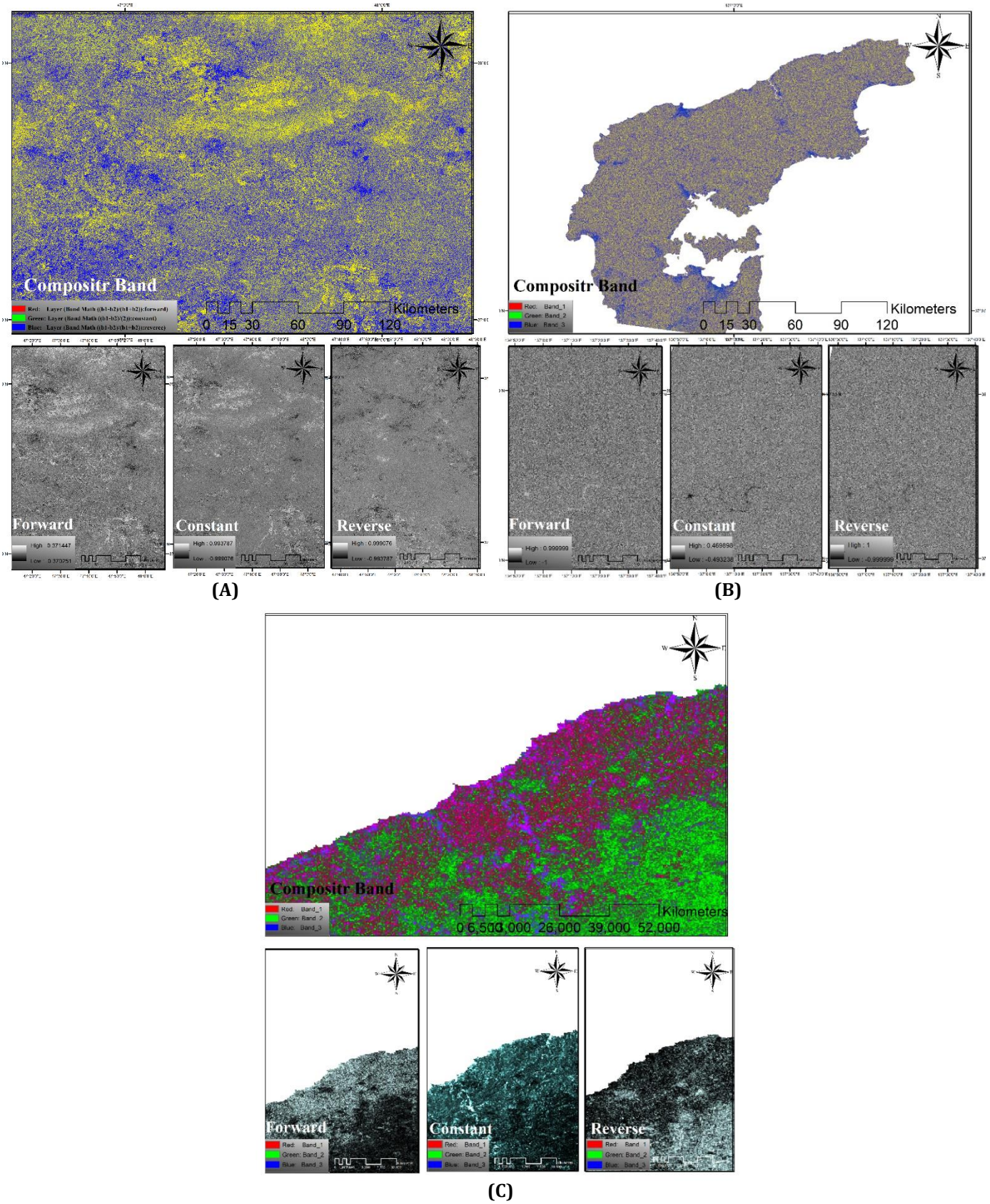

Figure 8. Change-detection outputs derived from Sentinel-1 and ALOS PALSAR-2 imagery: (A) Sentinel-1 for East Azerbaijan Province, Iran; (B) Sentinel-1 for Ishikawa Prefecture, Japan; and (C) ALOS PALSAR-2 for Ishikawa Prefecture, Japan, highlighting areas of significant surface and infrastructure changes following the earthquakes

Table 1. Statistical distribution and descriptive parameters of ALOS PALSAR-2 imagery for the Noto earthquake (Japan)

Satellite	Band	Processing Type	Minimum	Maximum	Mean	Standard Deviation	Acquisition Date
ALOS PALSAR-2	1	Input Image	0.00003	79.727371	0	0.114405	2022-11-22
ALOS PALSAR-2	2	Input Image	-60.348969	33.815189	0.116732	0.116191	2022-11-22
ALOS PALSAR-2	3	Input Image	-76.894569	34.337791	0	0.116236	2022-11-22
ALOS PALSAR-2	1	Input Image	0.00002	74.701866	0.00002	0.109083	2023-06-06
ALOS PALSAR-2	2	Input Image	-43.550808	53.242817	0.186432	0.107252	2023-06-06
ALOS PALSAR-2	3	Input Image	-44.551376	71.084864	0.117479	0.107338	2023-06-06
ALOS PALSAR-2	1	Input Image	0.00002	92.725685	0.188645	0.124947	2024-01-02
ALOS PALSAR-2	2	Input Image	-46.051376	66.337944	0.117509	0.120814	2024-01-02
ALOS PALSAR-2	3	Input Image	-38.563309	92.702164	-14.841339	0.121005	2024-01-02
ALOS PALSAR-2	1	Adaptive Filter Before Event	0.002818	0.973632	-13.023581	0.099875	-
ALOS PALSAR-2	1	Adaptive Filter After Event	0.000073	0.947899	-13.469853	0.074319	-
ALOS PALSAR-2	1	Coherence Before Event	0.002837	1	-0.000485	0.100175	-
ALOS PALSAR-2	1	Coherence After Event	0.00001	1	-0.000146	0.073424	-
ALOS PALSAR-2	1	Intensity Analysis	-81.824966	42.899452	-0.000104	7.457068	2022-11-22
ALOS PALSAR-2	1	Intensity Analysis	-79.852577	42.742172	-0.001133	5.834038	2023-06-06
ALOS PALSAR-2	1	Intensity Analysis	-87.730232	42.821125	0.000126	5.778118	2024-01-02
ALOS PALSAR-2	1	Interferogram Before Event	-3.141587	3.141592	-0.000084	1.805433	-
ALOS PALSAR-2	2	Interferogram Before Event	-330.204193	53.620613	0	0.158627	-
ALOS PALSAR-2	3	Interferogram Before Event	-218.178833	120.821365	0.116732	0.139888	-
ALOS PALSAR-2	1	Interferogram After Event	-3.141591	3.141592	0	1.810889	-
ALOS PALSAR-2	2	Interferogram After Event	-44.368706	419.773132	0.00002	0.193807	-
ALOS PALSAR-2	3	Interferogram After Event	-146.507645	65.034027	0.186432	0.000835	-

Table 2. Statistical analysis of Sentinel-1 imagery acquired over Ishikawa Prefecture (Japan) for the Noto earthquake sequence

Satellite	Band	Processing Type	Minimum	Maximum	Mean	Standard Deviation	Acquisition Date
Sentinel-1	1	Input Image	0	4606.583496	0.033963	0.631739	2022-11-12
Sentinel-1	1	Input Image	0	4832.481445	0.026647	0.611068	2023-06-04
Sentinel-1	1	Input Image	0	4011.688721	0.026962	0.552001	2024-01-18
Sentinel-1	1	Adaptive Filter Before Event	0.000017	0.999	0.249434	0.131816	-
Sentinel-1	1	Adaptive Filter After Event	0.000033	0.999	0.250124	0.129141	-
Sentinel-1	1	Coherence Before Event	0	1	0.249879	0.012873	-
Sentinel-1	1	Coherence After Event	0	1	0.251004	0.125975	-
Sentinel-1	1	Intensity Analysis	-81.824966	42.899452	-14.841339	7.457068	2022-11-12
Sentinel-1	1	Intensity Analysis	-79.852577	42.742172	-13.023581	5.834038	2023-06-04
Sentinel-1	1	Intensity Analysis	-87.730232	42.821125	-13.469853	5.778118	2024-01-18
Sentinel-1	1	Interferogram Before Event	-3.141592	3.141589	-0.000489	1.805433	-
Sentinel-1	2	Interferogram Before Event	-330.20401	53.620632	-0.000147	0.158627	-
Sentinel-1	3	Interferogram Before Event	-218.17897	120.821548	-0.000104	0.139888	-
Sentinel-1	1	Interferogram After Event	-3.14159	3.141591	-0.001119	1.81089	-
Sentinel-1	2	Interferogram After Event	-44.378578	419.651031	0.000126	0.193777	-
Sentinel-1	3	Interferogram After Event	-146.569321	64.986038	-0.000084	0.083518	-
Sentinel-1	1	Input Image	0	4606.583496	0.033963	0.631739	2022-11-12
Sentinel-1	1	Input Image	0	4832.481445	0.026647	0.611068	2023-06-04
Sentinel-1	1	Input Image	0	4011.688721	0.026962	0.552001	2024-01-18
Sentinel-1	1	Adaptive Filter Before Event	0.000017	0.999	0.249434	0.131816	-
Sentinel-1	1	Adaptive Filter After Event	0.000033	0.999	0.250124	0.129141	-
Sentinel-1	1	Coherence Before Event	0	1	0.249879	0.012873	-

Table 3. Statistical summary of Sentinel-1 imagery covering East Azerbaijan Province (Iran) during the 2019 Mianeh earthquake event

Satellite	Band	Processing Type	Minimum	Maximum	Mean	Standard Deviation	Acquisition Date
Sentinel-1	1	Input Image	0	23204216	0.025254	0.080969	2019-10-16
Sentinel-1	1	Input Image	0	310752808	0.031627	0.089409	2019-10-28
Sentinel-1	1	Input Image	0	33178186	0.023504	0.08732	2019-11-09
Sentinel-1	1	Adaptive Filter Before Event	0.000126	0.999	0.485057	0.137956	-
Sentinel-1	1	Adaptive Filter After Event	0.000008	0.999	0.469463	0.142002	-
Sentinel-1	1	Coherence Before Event	0.000001	1	0.483107	0.138198	-
Sentinel-1	1	Coherence After Event	0.000001	1	0.467051	0.141914	-
Sentinel-1	1	Intensity Analysis	-8374.7	2299721	-17.73549	4.137467	2019-10-16
Sentinel-1	1	Intensity Analysis	-9606.3	23388979	-16.639361	4.204883	2019-10-28
Sentinel-1	1	Intensity Analysis	-8003.3	24600315	-18.152736	4.194446	2019-11-09
Sentinel-1	1	Interferogram Before Event	-3.14159	3.141593	0.00042	1.742734	-
Sentinel-1	2	Interferogram Before Event	-293111	19411795	-0.000028	0.063128	-
Sentinel-1	3	Interferogram Before Event	-124347	197804718	0.000001	0.060418	-
Sentinel-1	1	Interferogram After Event	-3.14159	3.141593	0.000287	1.741393	-
Sentinel-1	2	Interferogram After Event	-252362	254833542	-0.000019	0.062049	-
Sentinel-1	3	Interferogram After Event	-329829	19116391	-0.000007	0.060764	-
Sentinel-1	1	Input Image	0	23204216	0.025254	0.080969	2019-10-16
Sentinel-1	1	Input Image	0	310752808	0.031627	0.089409	2019-10-28
Sentinel-1	1	Input Image	0	33178186	0.023504	0.08732	2019-11-09
Sentinel-1	1	Adaptive Filter Before Event	0.000126	0.999	0.485057	0.137956	-
Sentinel-1	1	Adaptive Filter After Event	0.000008	0.999	0.469463	0.142002	-
Sentinel-1	1	Coherence Before Event	0.000001	1	0.483107	0.138198	-

5. Discussion

The integration of Sentinel-1 and ALOS PALSAR-2 datasets facilitated a comprehensive and multi-scale assessment of infrastructure damage associated with the 2024 Noto and 2019 Mianeh earthquakes. By combining InSAR-derived coherence maps with radar backscatter intensity metrics, the spatial extent and severity of damage were delineated with high precision. Substantial reductions in coherence were observed across key infrastructure components—including highways, administrative facilities, and densely populated residential districts. For instance, coherence along major transportation corridors declined

from approximately 0.24 before the event to below 0.07 afterward, indicating significant structural instability and potential ground deformation.

The comparative evaluation of the two radar systems underscored their complementary sensing capabilities. ALOS PALSAR-2, with its longer L-band wavelength, proved highly effective in detecting large-scale deformation patterns and penetrating vegetated landscapes, thereby capturing broader spatial signatures of seismic activity. Conversely, the higher spatial resolution of the C-band Sentinel-1 system enabled the detection of fine-scale urban damages, including micro-cracking and localized subsidence, providing detailed insights into the vulnerability of built-up areas. The synergistic integration of both datasets markedly improved the reliability, completeness, and spatial detail of the damage assessment.

Consistent correspondence between coherence reductions and decreases in backscatter intensity further supported the robustness of the adopted methodological framework. The use of adaptive and Goldstein filtering techniques enhanced signal quality by suppressing noise while preserving critical structural information. These findings demonstrate strong alignment with previous studies that emphasize coherence loss as a key diagnostic indicator for post-seismic damage mapping and highlight the value of integrating SAR, optical, and GIS-based datasets to enhance assessment accuracy (Karimzadeh et al., 2018; Plank, 2014).

Despite these methodological advances, several operational limitations persist. The availability of pre-event SAR imagery with consistent acquisition geometry remains a major constraint and can affect the temporal comparability of interferometric products. Moreover, the development of rapid and fully automated workflows is necessary to support near-real-time monitoring and decision-making in the aftermath of seismic catastrophes. Addressing these constraints is essential for strengthening disaster response mechanisms, improving infrastructure resilience assessments, and informing long-term reconstruction strategies in seismically active regions.

6. Conclusions

This study demonstrates the effectiveness of multi-temporal radar observations—particularly Sentinel-1 (C-band) and ALOS PALSAR-2 (L-band)—for the rapid assessment of earthquake-induced damage to urban infrastructure following the 2024 Noto and 2019 Mianeh earthquakes. Variations in pre- and post-event backscatter intensity and interferometric coherence clearly revealed the spatial extent and severity of structural failures and ground deformations. Pronounced coherence reductions of up to 0.5 in critical infrastructures, together with backscatter decreases of approximately 10–15 dB in severely affected buildings, confirm the strong sensitivity of SAR measurements to seismic impacts.

The comparative analysis of C- and L-band datasets highlights their complementary capabilities. Sentinel-1 effectively captured fine-scale structural disturbances within dense urban environments, while the longer-wavelength ALOS PALSAR-2 system detected broad-scale ground deformation patterns that were less visible in C-band imagery. The integration of both radar systems provided a more complete, robust, and accurate representation of earthquake impacts. Additionally, the combination of coherence thresholding with visual inspection of interferograms enabled rapid delineation of heavily damaged zones with minimal preprocessing requirements.

Overall, the joint use of coherence and backscatter metrics from multi-source SAR datasets constitutes a reliable, rapid, and cost-efficient framework for post-earthquake damage assessment. This integrated approach enhances situational awareness for emergency response operations and supports evidence-based reconstruction planning in seismically active regions. Future work should focus on improving automation, precision, and operational readiness by incorporating high-resolution optical imagery, pre-event building inventories, and advanced machine learning or deep learning models. Such

enhancements will further strengthen the applicability and scalability of SAR-based damage assessment frameworks for real-time disaster management.

Acknowledgments: The authors would like to thank ESA (European Space Agency) and JAXA (Japan Aerospace Exploration Agency) for providing the SAR datasets. The second author also thanks Prof. Masashi Matsuoka from Science Tokyo for his valuable discussions.

Author Contributions:

F. Sanaei: Writing—original draft, Writing—review & editing, Validation, Software, Resources, Methodology, Investigation, Formal Analysis, Supervision, Conceptualization.

S. Karimzadeh: Writing—original draft, Writing—review & editing, Software, Resources, Methodology.

B. Feizizadeh: Writing—original draft, Writing—review & editing, Software, Resources, Methodology.

AI Contribution Statement: No artificial intelligence (AI) tools were used in the preparation of this manuscript. All work was conducted entirely by the authors.

Funding: This study received no external funding.

Research and publication ethics statement: In the study, the authors declare that there is no violation of research and publication ethics and that the study does not require ethics committee approval.

Conflicts of Interest: Sadra Karimzade, one of the co-authors of this manuscript, is a member of the journal's Editorial Board. All editorial handling and decisions were made independently,without his involvement. Apart from this, the authors declare no conflict of interest.

Data Availability: The data presented in this study can be provided upon request from the corresponding author.

References

Asian Disaster Reduction Center. (2012). Comparative study of disaster management of Japan and Kyrgyz Republic. Asian Disaster Reduction Center. Retrieved September 12, 2025, from http://www.adrc.asia/aboutus/vrdata/finalreport/2012A_KGZ_fr.pdf

Asian Disaster Reduction Center. (2024). Disaster information: 2024 Noto Peninsula earthquake. Asian Disaster Reduction Center. Retrieved September 12, 2025, from https://www.adrc.asia

Arciniegas, G. A., Bijker, W., Kerle, N., & Tolpekin, V. A. (2007). Coherence- and amplitude-based analysis of seismogenic damage in Bam, Iran, using ENVISAT ASAR data. *IEEE Transactions on Geoscience and Remote Sensing*, 45(6), 1571–1581. https://doi.org/10.1109/TGRS.2006.883149

Azad, S., Saboor, N., Moradi, M., Ajhdari, A., Youssefi, T., Mashal, M., & Roustaei, M. (2017). Preliminary report on geological features of the Ezgaleh–Kermanshah earthquake (Mw 7.3), November 12, 2017, West Iran (SSD of GSI Preliminary Report No. 17-01, Ver. 01).

Bai, Y., Adriano, B., Mas, E., & Koshimura, S. (2017). Machine learning based building damage mapping from the ALOS-2/PALSAR-2 SAR imagery: Case study of the 2016 Kumamoto earthquake. *Journal of Disaster Research*, 12(4), 646–655. https://doi.org/10.20965/jdr.2017.p0646

Castriotta, A. G. (2017). Sentinel data access annual report of 2016 (Issue 1). European Space Agency.

Conroy, G. (2024). Japan earthquakes: The science behind deadly tremors. *Nature*, 625, 228. https://doi.org/10.1038/d41586-024-00010-1

Copernicus EMS. (2024). EMSR mapping products for the Noto Peninsula earthquake (Japan). Retrieved June 5, 2024, from https://emergency.copernicus.eu/mapping/list-of-activations/

Dong, L., & Shan, J. (2013). A comprehensive review of earthquake-induced building damage detection with remote sensing techniques. *ISPRS Journal of Photogrammetry and Remote Sensing*, 84, 85–99. https://doi.org/10.1016/j.isprsjprs.2013.06.011

Fielding, E. J., Talebian, M., Rosen, P. A., Nazari, H., Jackson, J. A., Ghorashi, M., & Walker, R. (2005). Surface ruptures and building damage of the 2003 Bam, Iran, earthquake mapped by satellite synthetic aperture radar interferometric correlation. *Journal of Geophysical Research: Solid Earth*, 110(B3). https://doi.org/10.1029/2004JB003299

Franceschetti, G., & Lanari, R. (1999). Synthetic aperture radar processing. CRC Press.

Gabriel, A. K., Goldstein, R. M., & Zebker, H. A. (1989). Mapping small elevation changes over large areas: Differential radar interferometry. *Journal of Geophysical Research,* 94(B7), 9183–9191. https://doi.org/10.1029/JB094iB07p09183

Gens, R., & van Genderen, J. L. (1996). SAR interferometry—issues, techniques, applications. *International Journal of Remote Sensing*, 17(10), 1803–1835. https://doi.org/10.1080/01431169608948741

Hoffmann, J. (2007). Mapping damage during the Bam (Iran) earthquake using interferometric coherence. *International Journal of Remote Sensing,* 28(6), 1199–1216. https://doi.org/10.1080/01431160600928567

Jackson, J. (1992). Partitioning of strike-slip and convergent motion between Eurasia and Arabia in eastern Turkey and the Caucasus. *Journal of Geophysical Research: Solid Earth*, 97(B9), 12471–12479. https://doi.org/10.1029/92JB00944

Japan Aerospace Exploration Agency. (2024). Disaster damage assessment with Earth observation satellite regarding the 2024 Noto Peninsula earthquake. Earth Observation Research Center (EORC), JAXA. Retrieved June 5, 2024, from https://www.satnavi.jaxa.jp/en/news/2024/05/14/9277/index.html

Karimzadeh, S., & Matsuoka, M. (2017). Building damage assessment using multisensor dual-polarized synthetic aperture radar data for the 2016 M 6.2 Amatrice earthquake, Italy. *Remote Sensing*, 9(4), 330. https://doi.org/10.3390/rs9040330

Karimzadeh, S., & Matsuoka, M. (2018). Building damage characterization for the 2016 Amatrice earthquake using ascending–descending COSMO-SkyMed data and topographic position index. *IEEE Journal of Selected Topics in Applied Earth Observations and Remote Sensing,* 11(8), 2668–2682. https://doi.org/10.1109/JSTARS.2018.2825399

Karimzadeh, S., Matsuoka, M., Miyajima, M., Adriano, B., Fallahi, A., & Karashi, J. (2018). Sequential SAR coherence method for the monitoring of buildings in Sarpole-Zahab, Iran. *Remote Sensing*, 10(8), 1255. https://doi.org/10.3390/rs10081255

Karimzadeh, S., Miyajima, M., Hassanzadeh, R., Amiraslanzadeh, R., & Kamel, B. (2014). A GIS-based seismic hazard, building vulnerability and human loss assessment for the earthquake scenario in Tabriz. *Soil Dynamics and Earthquake Engineering*, 66, 263–280. https://doi.org/10.1016/j.soildyn.2014.06.026

Lu, Z. (2007). InSAR imaging of volcanic deformation over cloud-prone areas: Aleutian Islands. P*hotogrammetric Engineering & Remote Sensing,* 73(3), 245–257. https://doi.org/10.14358/PERS.73.3.245

Matsuoka, M., & Nojima, N. (2010). Building damage estimation by integration of seismic intensity information and satellite L-band SAR imagery. *Remote Sensing*, 2(9), 2111–2126. https://doi.org/10.3390/rs2092111

Matsuoka, M., & Yamazaki, F. (2004). Use of satellite SAR intensity imagery for detecting building areas damaged due to earthquakes. *Earthquake Spectra*, 20(3), 975–994. https://doi.org/10.1193/1.1774182

Matsuoka, M., & Yamazaki, F. (2005). Building damage mapping of the 2003 Bam, Iran, earthquake using ENVISAT/ASAR intensity imagery. *Earthquake Spectra*, 21(S1), S285–S294. https://doi.org/10.1193/1.2101027

Matsuoka, M., & Yamazaki, F. (2006). Use of SAR imagery for monitoring areas damaged due to the 2006 Mid Java, Indonesia earthquake. Proceedings of the 4th International Workshop on Remote Sensing for Post-Disaster Response, Cambridge, Kingdom, 1–5.

Miyajima, M., Fallahi, A., Ikemoto, T., Samaei, M., Karimzadeh, S., Setiawan, H., Talebi, F., & Karashi, J. (2018). Site investigation of the Sarpole-Zahab earthquake, Mw 7.3 in SW Iran of November 12, 2017. *JSCE Disaster Fact Sheet Series* (FS2018-E-0002), 1–11.

Miura, H., Midorikawa, S., & Matsuoka, M. (2016). Building damage assessment using high-resolution satellite SAR images of the 2010 Haiti earthquake. *Earthquake Spectra*, 32(1), 591–610. https://doi.org/10.1193/033014EQS042M

NASA Earth Observatory. (2024). Earthquake lifts the Noto Peninsula (Ground deformation from the Noto earthquake captured by radar). Retrieved June 5, 2024, from https://earthobservatory.nasa.gov/images/152350/earthquake-lifts-the-noto-peninsula

Nishimura, T., Hiramatsu, Y., & Ohta, Y. (2023). Episodic transient deformation revealed by the analysis of multiple GNSS networks in the Noto Peninsula, central Japan. *Scientific Reports*, 13, 8381. https://doi.org/10.1038/s41598-023-35454-z

Peykani, O. (2021). Earthquake resilience of settlements in Mianeh County (Case study: Turkmenchay City and Varzeghan Village). Proceedings of the Fourth National Conference on Knowledge-Based Urban Planning and Architecture. Iran.

Plank, S. (2014). Rapid damage assessment by means of multi-temporal SAR: A comprehensive review and outlook to Sentinel-1. *Remote Sensing,* 6(6), 4870–4906. https://doi.org/10.3390/rs6064870

Strozzi, T., Dammer, P. B. G., Wegmüller, U., Martinez, J.-M., Askne, J. I. H., Beaudoin, A., & Hallikainen, M. T. (2000). Land-use mapping with ERS SAR interferometry. *IEEE Transactions on Geoscience and Remote Sensing*, 38(2), 766–775. https://doi.org/10.1109/36.842005

Takeuchi, S., Suga, Y., Yonezawa, C., & Chen, A. J. (2000). Detection of urban disaster using InSAR: A case study for the 1999 Great Taiwan earthquake. In Proceedings of the IEEE International Geoscience and Remote Sensing Symposium (IGARSS 2000), Honolulu, HI, United States, 339–341.

UNOSAT. (2023). Earthquake damage assessment overview: Noto, Japan. United Nations Satellite Centre (UNITAR). Retrieved September 9, 2023, from https://unosat.org

Vidale, J. E., & Shearer, P. M. (2006). A survey of 71 earthquake bursts across southern California: Exploring the role of pore fluid pressure fluctuations and aseismic slip as drivers. *Journal of Geophysical Research: Solid Earth,* 111(B5), B05312. https://doi.org/10.1029/2005JB004034

Wang, Q.-Y., Cui, X., Frank, W. B., Lu, Y., Hirose, T., & Obara, K. (2024). Untangling the environmental and tectonic drivers of the Noto earthquake swarm in Japan. *Science Advances*, 10(19), eado1469. https://doi.org/10.1126/sciadv.ado1469

Watanabe, M., Motohka, T., Miyagi, Y., Yonezawa, C., & Shimada, M. (2012). Analysis of urban areas affected by the 2011 off the Pacific coast of Tohoku earthquake and tsunami with L-band SAR full-polarimetric mode. *IEEE Geoscience and Remote Sensing Letters*, 9(3), 472–476. https://doi.org/10.1109/LGRS.2011.2182030

Watanabe, M., Thapa, R. B., Ohsumi, T., Fujiwara, H., Yonezawa, C., Tomii, N., & Suzuki, S. (2016). Detection of damaged urban areas using interferometric SAR coherence change with PALSAR-2. *Earth, Planets and Space*, 68, 131. https://doi.org/10.1186/s40623-016-0513-2

Yamazaki, F., Matsuoka, M., & Muraoka, N. (2005). Remote sensing technologies for post-earthquake damage assessment: A case study of the 2003 Bam earthquake. *Journal of Earthquake Engineering*, 9(Suppl. 1), 195–209. https://doi.org/10.1142/S1363246905002394

Yonezawa, C., & Takeuchi, S. (2001). Decorrelation of SAR data by urban damages caused by the 1995 Hyogoken-Nanbu earthquake. *International Journal of Remote Sensing*, 22(8), 1585–1600. https://doi.org/10.1080/01431160118187

Zebker, H. A., & Villasenor, J. (1992). Decorrelation in interferometric radar echoes. *IEEE Transactions on Geoscience and Remote Sensing*, 30(5), 950–959. https://doi.org/10.1109/36.175330

Zheng, Z., Zhong, Y., Wang, J., Ma, A., & Zhang, L. (2021). Building damage assessment for rapid disaster response with a deep object-based semantic change detection framework: From natural disasters to man-made disasters. *Remote Sensing of Environment*, 265, 112636. https://doi.org/10.1016/j.rse.2021.112636